Journal of Metals, Materials and Minerals, 36(1), e2422, 2026

Effects of welding currents on microstructure and corrosion behaviors of Inconel 625 cladding on 2.25Cr-1Mo steel by Hot-wire TIG

Supparat SAEHENG[1], Hein Zaw OO[1], and Prapas MUANGJUNBUREE[1,2,*]

[1] *Department of Mining and Materials Engineering, Faculty of Engineering, Prince of Songkla University, Hat Yai, Songkhla, 90110, Thailand*
[2] *Center for Sustainable and Advanced Materials (CSAM), Faculty of Engineering, Prince of Songkla University, Hat Yai, Songkhla, 90110, Thailand*

***Corresponding author e-mail**: prapas.m@psu.ac.th

Received date:
3 June 2025
Revised date:
18 August 2025
Accepted date:
24 September 2025

Keywords:
2.25Cr-1Mo steel;
Inconel 625;
Hot-wire TIG;
Cladding;
Corrosion behaviors

Abstract

Hot-wire tungsten inert gas (HW-TIG) cladding has been applied to the steam turbine rotor welding repair. This study investigated the effects of welding currents on microstructure, hardness, and corrosion behavior. The experiments were conducted using four different welding currents applied to bead-on-plate Inconel 625 welds on a 2.25Cr-1Mo steel substrate as the steam turbine rotor material. The selected welding currents were 125 A, 150 A, 175 A, and 200 A. The percentages of weld dilution for different welding currents were also evaluated. Higher welding currents increased weld dilution, weld bead width, and HAZ size. As the welding current increased, the nickel alloy weld metal became more diluted with the base metal. The microstructure of the weld metal was a dendritic austenite phase. The weld metal exhibited the highest hardness at 150 A, with an average of 240 $HV_{0.2}$. And the lowest hardness at 200 A, with an average of 195 $HV_{0.2}$. The electrochemical corrosion test performed in a 3.5% NaCl solution showed that the corrosion rate was lowest in the weld metal at 150 A. According to the analytical results, a welding current of 150 A was found to be the most suitable for repairing steam turbine rotors using the HW-TIG process.

1. Introduction

The expansion of renewable energy sources is significantly impacting conventional thermal power plants [1]. To smooth out power inconsistencies, these plants are forced into more frequent turbine cycling (starting and stopping), faster power adjustments, and operating at elevated temperatures. This heavy workload ultimately diminishes the operational life of their steam turbines [2]. High thermal and mechanical stress cause a significant threat to the integrity and useful life of crucial turbine rotating components like rotors [3]. Over long periods of operation in complex environments, the efficiency of equipment is compromised by the growth of defects, ultimately leading to a potential loss of functionality [4].

Rubbing between the spinning and fixed parts of a steam turbine is a common operational issue [5]. This rubbing can cause the turbine's rotor to vibrate in very complicated ways. While minor cases might only result in severe unit vibration, more serious rubbing can lead to permanent bending of the rotor or even the complete failure of the shaft assembly [6]. Significant replacement costs can be avoided if defects are identified and addressed in their initial stages, eliminating the need for full part replacement [7]. Consequently, once defects are identified on the rotor's surface, a suitable repair technique must be implemented to preserve the rotor.

Overlay welding, also known as cladding, is the preferred solution over complete replacement of damaged parts [8]. Overlay welding repair is a technique that restores damaged components to their original form by melting and depositing alloy materials onto their surface [9]. This approach is favored due to its quicker turnaround time and lower cost [10]. Additionally, welding offers effective solutions for both upgrading and repairing existing steam turbine rotors [11]. Tungsten inert gas (TIG) welding process is a popular choice to repair the turbine rotors and turbine blades [12]. It offers excellent microstructural quality and allows for independent control over the heat input and the deposition rate. Furthermore, TIG equipment is relatively inexpensive, the process can be automated with ease, and it's compatible with a wide range of materials [13].

TIG welding is characterized by its stability of arc and absence of spatter because its arc is independently ignited by a non-consumable tungsten electrode [14]. Additionally, the use of shielding gas enables this technique to be effectively utilized on a broad spectrum of metals and alloys, even those that are highly reactive [15]. However, a notable disadvantage of TIG is its inherently low deposition rate due to the non-consumable nature of the electrode. To address this limitation, hot-wire tungsten inert gas (HW-TIG) was introduced [16]. In this advanced method, the filler wire is preheated to a temperature range of 300°C to 500°C before it is fed into the weld pool. This preheating significantly enhances the deposition rate in comparison to conventional cold-wire TIG [17]. Since the filler wire is preheated before entering the weld pool, it requires less energy from the welding arc to melt. This mechanism accelerates the melting of filler metals and increases the overall deposition rate compared to standard TIG [18]. The HW-TIG technique, particularly when implemented using robotic systems, has

DOI:10.55713/jmmm.v36i1.2422

emerged as an advanced method for improving weld quality and minimizing production costs [19]. This process offers significant advantages, particularly its low dilution rate and high deposition rate, which effectively contribute to shortened production times [20,21]. Compared with conventional TIG welding, HW-TIG generates a deeper and narrower weld pool due to increased heat input and deposition speed, enhancing both efficiency and weld quality [22,23].

Steam turbine rotors are typically manufactured from low-alloy steels such as CrMoV (ASTM A470 Class 8) and NiCrMoV (ASTM A470 Class 6), owing to their strength and high-temperature resistance [4,10]. The 2.25Cr-1Mo alloy, classified as ASTM Grade 22, is a low-alloy steel with a ferritic-bainitic microstructure, originally designed for use in high-temperature environments [24]. It is very important to carefully consider the selection of appropriate filler materials for repairing steam turbine rotors. As a nickel-based superalloy, Inconel 625 stands out as a high-performance alloy, demonstrating remarkable capabilities such as superior mechanical strength and corrosion resistance [25]. For uses requiring both significant strength and corrosion resistance, like low-pressure turbines, Inconel 625 is frequently chosen for its performance in the medium temperature range of 250°C to 593°C [26].

Elango and Balaguru [27] investigated Inconel 625 weld overlay on carbon steel using the Gas Metal Arc Welding (GMAW) process to improve corrosion resistance in applications of the oil and petrochemical industries. They studied the weld overlay with controlled parameters, including specific current, voltage, and shielding gas mixture, and then analyzing the weld's properties such as chemical composition, hardness, and cracking tendencies. The results indicated that a good weld bead was achievable with controlled parameters and low iron content, demonstrating improved strength and corrosion resistance compared to the base metal. Alvaraes *et al.* [28] evaluated the microstructure and corrosion characteristics of a single-layer Inconel 625 weld cladding deposited by the electroslag welding (ESW) process on an ASTM A516 Gr. 70 steel plate. This study found the effects of different distances (1 mm and 3 mm) from the fusion line on corrosion results and microstructure of cladding. In a study by Kim *et al.* [29], the influences of welding heat input on the microstructure and pitting corrosion resistance of electroslag-welded Inconel 625 overlay welds were examined. Although increased heat input led to a broader melted zone near the fusion line, corrosion resistance didn't significantly differ between specimens. This consistency was likely due to the low dilution rate at the surface, which ensured the surface compositions were nearly identical, regardless of the heat input variations. According to Park *et al.* [30], this study introduced the novel super-TIG welding method using a C-type Inconel 625 filler to analyze the relationships between the heat input and bead geometry for both stringer and oscillation bead-on-plate welds on SS400 steel. They observed that heat input significantly affects weld characteristics, specifically the molten pool length, penetration depth, and bead height.

Many studies have shown that increasing the filler wire temperature leads to wider welds with reduced reinforcement, indicating improved surface coating efficiency [31,32]. Silwal *et al.* found that surface cladding using Inconel 625 filler wire on stainless steel 347 with HW-TIG at low current ranges (60 A to 100 A) demonstrated optimal bead formation and low dilution at welding angles between 65° and 80° [33]. Similarly, in accordance with Evangelin *et al.*, cladding Inconel 625 onto AISI 316L revealed that increased welding current enhances penetration depth while reducing reinforcement, whereas increased travel speed reduces dilution and bead width [34].

There is no previous research that has studied the corrosion resistance of a single-bead Inconel 625 weld on a 2.25Cr-1Mo substrate deposited by HW-TIG process. This study directly addresses this gap by investigating how varying welding currents in the HW-TIG process influence the properties of Inconel 625 cladding on a 2.25Cr-1Mo substrate. In this study, effects of varying welding currents on weld bead geometry, weld dilution, chemical composition, microstructure, hardness and corrosion resistance were systematically studied to determine the suitable welding parameters to repair the turbine rotor using HW-TIG process.

2. Experimental procedures

2.1 Materials

A chromium-molybdenum alloy steel plate (steam turbine rotor material), specifically ASTM A387 Gr.22 (containing 2.25% chromium and 1% molybdenum), was used as the base metal for surface cladding. The cladding was done using Inconel 625 welding wire. The chemical composition of both the base metal and the welding electrode is shown in Table 1.

2.2 Methodology

In the HW-TIG welding process, the filler wire is preheated by passing an electric current through it to assist in its melting. The filler wire can be fed using an automatic wire feeder, as illustrated in Figure 1. Single weld beads were deposited onto 2.25Cr-1Mo steel plates (250 mm × 120 mm × 15 mm) at varying welding currents of 125 A, 150 A, 175 A, and 200 A, as shown in Figure 2. An ATIG400P (HW) welding machine was used with Inconel 625 welding wire (1.2 mm diameter) and a hot wire current of 70 A. The constant welding parameters used for the four samples welded with varying currents in this study were as follows: voltage of 15 V, welding speed of 12 cm·min^{-1}, wire feed speed of 0.6 m·min^{-1}, welding angle of 60°, and shielding gas flow rate of 15 L·min^{-1}. Pure argon gas was used as the shielding gas for all conditions. The calculated heat inputs for the varying welding currents are listed in Table 2. Heat inputs were calculated by Equation (1) and Equation (2) [35].

Table 1. Chemical composition of base metal (2.25Cr-1Mo) and Inconel 625 filler wire.

Material	**Chemical composition [wt%]**												
	C	**Si**	**Mn**	**P**	**S**	**Ni**	**Cr**	**Mo**	**Co**	**Ti**	**Al**	**Nb**	**Fe**
2.25Cr-1Mo	0.05-0.15	0.5	0.3-0.6	0.025	0.025	-	1.9-2.6	0.87-1.13	-	-	-	-	Bal.
Inconel 625	0.1	0.5	0.5	0.015	0.015	Bal.	20-23	8-10	1	0.4	0.4	3.15-4.15	5

Table 2. Calculated Heat Inputs for Varying Welding Currents.

Welding current [A]	**Heat Input [kJ·mm^{-1}]**
125 A	1.27
150 A	1.46
175 A	1.65
200 A	1.84

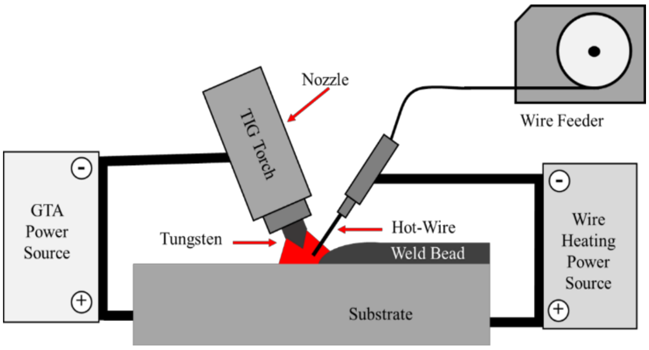

Figure 1. Schematic diagram of HW-TIG.

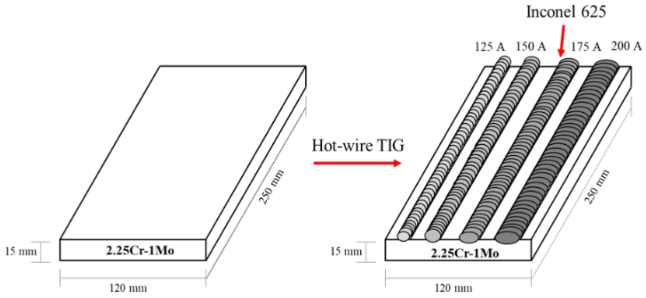

Figure 2. Schematic drawing of single-bead HW-TIG cladding on 2.25Cr-1Mo steel plate.

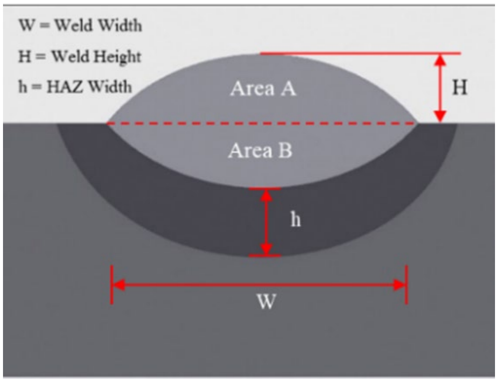

Figure 3. Schematic diagram illustrating single weld bead characteristics.

$$\text{Heat Input} = \frac{(I_w^2 \times R_w)}{v_w} + \frac{(VI)}{v} \qquad (1)$$

Where

I = Welding current (A)
V = Voltage (V)
v = Welding speed (cm·min^{-1})
I_w = Welding wire current (A)
v_w = Wire feed speed (m·min^{-1})
R_w = Resistance of wire (Ω)

$$R_w = \frac{\rho L}{A_w} \qquad (2)$$

Where

ρ = Resistivity (Ω·m)
L = Extension length of the filler wire (m)
A_w = Cross-sectional area of the filler wire (m^2)

2.3 Macro/microstructure investigation

Specimens welded with Inconel 625 filler metal on 2.25Cr-1Mo steel were prepared for testing under varying welding current conditions. The cross-sectional macrostructures of the welds were sectioned and progressively ground using abrasive papers with grit sizes of 180, 240, 360, 400, 600, 800, 1200, and 2500. Subsequent polishing was performed using a 3 µm diamond suspension. Metallographic etching was carried out using two different reagents: a 2% Nital solution for 10 s to reveal the microstructure of the base metal and a mixture of HCl and HNO_3 in a 4:1 ratio for 30 s to etch the Inconel 625 weld metal.

The prepared specimens were examined for macrostructural characteristics using a stereo microscope. Measurements of weld bead width, heat-affected zone (HAZ) width, and weld bead height were measured, as depicted in Figure 3. Additionally, the dilution ratio between the weld metal and base metal was determined using Equation (3).

For microstructural analysis, an optical microscope was employed to examine the weld metal and HAZ under different welding conditions. The microstructural assessment of the weld metal was conducted at three specific regions: the top surface, the center of the weld bead, and the interface between the weld metal and the HAZ. The microstructure of the heat-affected zones (HAZs) was analyzed in two distinct regions: the coarse-grained heat-affected zone (CGHAZ) and the fine-grained heat-affected zone (FGHAZ). Furthermore, the elemental composition of the weld metal was analyzed using a portable X-ray fluorescence (XRF) spectrometer, with X-ray beams directed onto the top surface of the weld bead to identify the chemical composition of the alloying elements.

$$\text{Weld dilution} = \frac{\text{Area B}}{\text{Area A} + \text{Area B}} \times 100\% \qquad (3)$$

2.4 Hardness measurement

Microhardness profiles were evaluated across the weld metal, heat-affected zone (HAZ), base metal, and the top surface of the weld bead using a micro-Vickers hardness tester. A load of 200 gf was applied for 10 s, with measurements recorded at 0.2 mm intervals along the cross-section of the welded samples. For each welding current, hardness was assessed at ten randomly selected points on the weld bead's top surface. The measurements were conducted sequentially, starting from the weld metal, moving through the HAZ, and extending into the base metal, as illustrated in Figure 4.

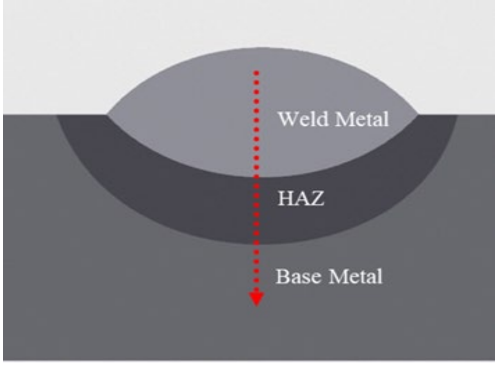

Figure 4. Hardness measurement locations across the weld bead cross-section.

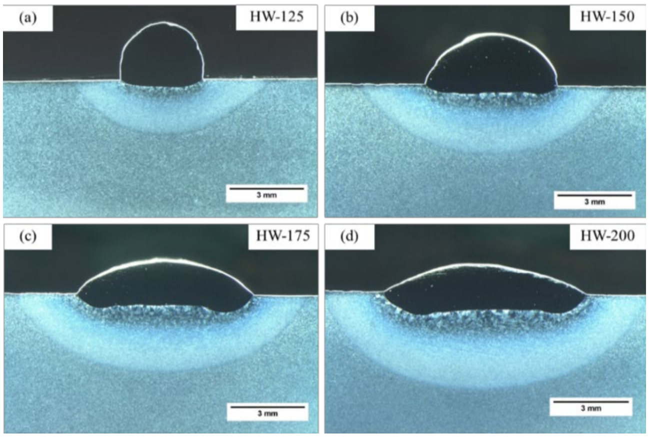

Figure 5. The cross-sectional macrostructure at different welding currents (a) 125 A, (b) 150 A, (c) 175 A, and (d) 200 A.

2.5 Electrochemical corrosion testing

Electrochemical corrosion tests were performed on the weld metal using an Auto-Lab potentiostat controlled by NOVA 2.1.5 software. The samples were prepared by cold-mounting, grinding, and polishing to a 3 µm surface finish. A 0.0491 cm^2 circular area of the weld metal was exposed for testing, with the remaining surface masked. A standard three-electrode setup was employed, consisting of a platinum counter electrode, an Ag/AgCl reference electrode, and the weld sample as the working electrode. The exposed area was immersed in a 0.6 M NaCl (equivalent to 3.5% NaCl) solution at room temperature. Linear polarization measurements were recorded over a 5400 s period.

3. Results and discussion

3.1 Macrostructure

The physical characteristics of the weld bead, including weld bead width, weld bead height, HAZ size, and weld dilution percentage, are assessed through macrostructural analysis. The macrostructure of single weld beads, produced under varying welding currents, is presented in Figure 5. According to the macrographs, higher currents lead to enhanced melting of both the filler and base metal, resulting in a broader molten pool and, consequently, a wider bead and HAZ.

3.2 Dilution

Weld dilution for each welding condition was measured using macrographs. The measured dilution percentages for the welds deposited at 125 A, 150 A, 175 A, and 200 A were 10%, 15%, 32%, and 46%, respectively. These results demonstrate a significant correlation between welding current and dilution percentage. As the welding current increases from 125 A to 200 A, the dilution percentage significantly rises from 10% to 46%. This trend is expected, as higher currents generally lead to greater heat input, resulting in more extensive melting of the base metal and consequently higher dilution. As shown in Table 3, higher welding currents are associated with increased dilution percentage, weld bead width, and HAZ size, but decreased weld bead height. A higher heat input resulted in slower cooling rates, which affected the elevated temperatures, thereby increasing the width of the HAZ [35]. Figure 6 illustrates the effect of primary current on clad bead dimensions, including width, height, and HAZ size, as well as dilution.

3.3 X-ray fluorescence (XRF) analysis

The elemental analysis of weld beads using X-ray fluorescence (XRF) revealed that the concentrations of chemical elements in the Inconel 625 weld metal decreased when the welding current increased. The XRF results are shown in Table 4. Between welding currents of 125A and 200A, nickel content decreases from 56.14% to 34.06%, while chromium drops from 20.92% to 12.64%. Molybdenum reduces from 7.79% to 5.22%, whereas iron increases significantly from 9.93% to 44.48%. These results demonstrate that increased welding currents resulted in higher dilution rates, consequently altering the chemical composition of the alloys. This resulted in decreased concentrations

Table 3. Weld dilution and measurement of the bead weld size.

Sample	Weld dilution	Weld width [W]	Weld height [H]	HAZ width [h]
HW-125	10%	3.3 mm	2.4 mm	2.0 mm
HW-150	15%	5.3 mm	2.1mm	2.5 mm
HW-175	32%	7.1 mm	1.5 mm	2.8 mm
HW-200	46%	8.2 mm	1.2 mm	3.2 mm

Table 4. Chemical composition of weld beads analyzed by X-ray fluorescence (XRF).

Samples	Chemical composition [wt%]										
	Mn	Si	Ni	Cr	Mo	Fe	P	S	Ti	Nb	V
HW-125	0.35	0.30	56.14	20.92	7.79	9.93	0.06	0.84	0.26	3.11	0.01
HW-150	0.30	0.26	53.77	20.14	7.54	13.49	0.05	0.70	0.44	3.03	0.01
HW-175	0.38	0.25	44.09	17.04	6.27	28.09	0.04	0.62	0.46	2.50	0.01
HW-200	0.26	0.28	34.06	12.64	5.22	44.48	0.06	0.40	0.17	2.06	-

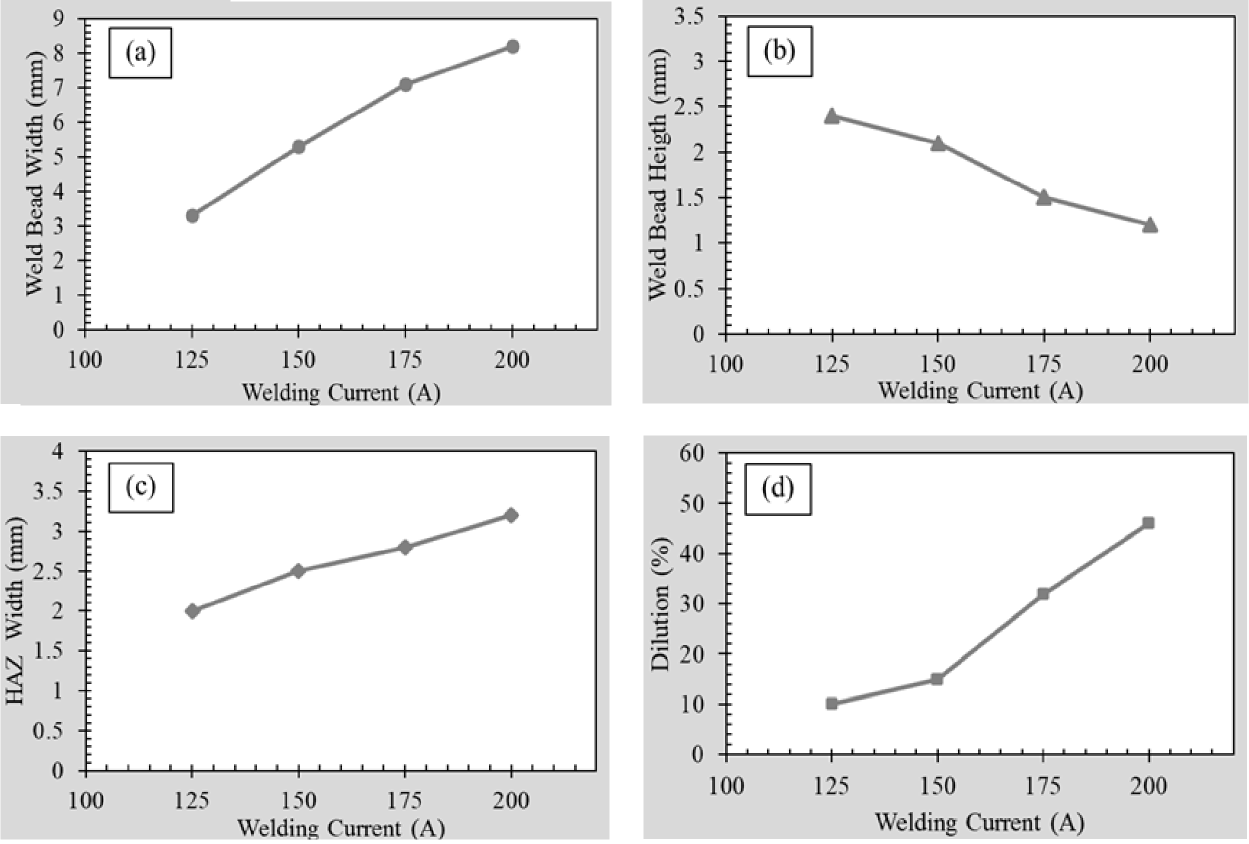

Figure 6. Effect of welding currents on clad bead dimensions and dilution.

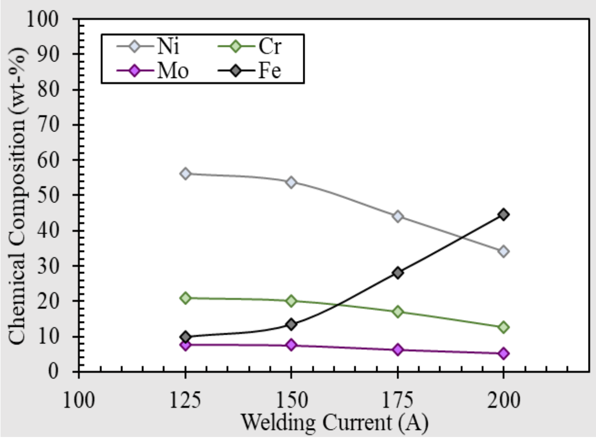

Figure 7. Effect of welding current on composition of chemical elements in the weld beads.

Figure 7 shows the effect of welding current on the chemical composition of a weld bead, showing the variation in Ni, Cr, Mo, and Fe concentrations as the welding current increases from 125 A to 200 A. The graph illustrates the effect of welding current on the chemical composition of a weld bead. As the welding current increases, the concentrations of Nickel (Ni) and Chromium (Cr) decrease, while the concentration of Iron (Fe) increases. This suggests that higher welding currents lead to greater dilution of the weld metal with the base metal, which likely has a higher iron content. Molybdenum (Mo) content remains relatively constant across all welding currents. This trend indicates that the dilution effect is primarily influencing the concentrations of Ni, Cr, and Fe. The chemical composition of the HW-150 sample exhibits minimal differences in nickel, chromium, molybdenum, and iron content when compared to the sample produced at 125A. Consequently, the HW-150 sample exhibited the optimal chemical composition.

3.4 Optical microstructure analysis

The microstructure of the coarse grain heat affected zone (CGHAZ) located near the fusion line is shown in Figure 8. The average grain sizes in the CGHAZ for welding currents of 125 A, 150 A, 175 A, and 200 A are recorded as 54.03 µm, 58.65 µm, 61.85 µm, and 73.54 µm, respectively. Bainite phase appeared in the CGHAZ of each condition. The CGHAZ exhibited a coarser grain structure compared to the FGHAZ due to its exposure to higher peak temperatures during the welding process, resulting in slower cooling rates, and it was located closer to the weld interface. These elevated temperatures facilitated the complete dissolution of precipitates, eliminating any barriers to grain growth in this region [37].

Figure 9 depicts the microstructure of the fine-grained heat-affected zone (FGHAZ) situated adjacent to the CGHAZ. The FGHAZ exhibits relatively stable grain size across the four different welding currents. At four different welding currents, the average grain sizes in the FGHAZ are 11.39 µm, 11.49 µm, 11.54 µm, and 14.91 µm, respectively. This region exhibits bainitic structures with a finer grain size. The rapid cooling rates experienced in this zone and the associated thermal gradients promote the formation of a refined grain structure.

The microstructure of the weld metals in cross-section at the top, center, and bottom near the fusion line is presented in Figure 10. The microstructure observed on the top area of the weld metal revealed a dendritic austenite structure consisting of equiaxed dendrites. The presence of a high nickel concentration in the Inconel 625 weld metal favoured the stabilization of the austenite phase. Compared to the weld interface, the lowest temperature gradient on the top region of the single weld bead resulted in the formation of equiaxed grains [38]. At lower currents (125 A and 150 A), the top region displays fine equiaxed dendritic structures due to a high cooling rate. In contrast, at higher currents (175 A and 200 A), the dendritic morphology becomes coarser and more irregular, reflecting slower solidification conditions due to increased heat input. Specifically, the liquid metal at the top of the weld pool experienced heat transfer not only through conduction into the base metal but also via convective and radiative losses to the surrounding shielding gas. This additional cooling pathway, coupled with the enhanced convective cooling due to the shielding gas flow, increased the overall solidification rate. The faster solidification kinetics promoted nucleation overgrowth, and the multi-directional heat flow prevented the establishment of a strong temperature gradient, leading to the formation of the randomly oriented, fine equiaxed dendrites rather than a columnar grain structure [39]. The center region across all current levels consistently shows columnar dendritic structures growing epitaxially from the fusion line, with the degree of elongation and grain coarseness increasing with current. The grain structure shows a clear columnar morphology growing in the direction of heat extraction [40]. In the central area, at 125 A and 150 A, the dendritic arms are thinner and more compact. At 175 A and 200 A, the columnar grains are wider, and secondary arm coarsening is observed, suggesting a reduced thermal gradient and an increased growth rate [41]. The bottom region adjacent to the base metal shows epitaxial columnar growth [42], with a HAZ visible under the fusion line. At 125 A of the bottom area, the columnar grains are thin and well-aligned, indicating higher cooling rates at the interface. As current increases, there is a significant thickening of the columnar grains. The welding of 200 A shows the most coarsened grains with a less distinct transition zone between the fusion zone and base metal, implying a much higher heat input and slower solidification rate at the interface. The dark region at the bottom may indicate HAZ. Dendrite growth with a coarser increased with increasing welding current, primarily due to the slower cooling rates associated with higher currents [43].

The austenitic structure is observed in the form of equiaxial dendrites at the top surface, as presented in Figure 11. The structure is consistent with the cross-section in the upper part, which shows the effect of welding current on the microstructure regarding shape and size. At the lowest welding current of 125 A, the microstructure reveals coarse dendritic phases with wide dendritic arm spacing. As the current increases to 150 A, the dendritic phases become slightly refined, and the dendritic arm spacing decreases compared to the microstructure at 125 A. The dendritic arms become more numerous, and the spacing between them reduces. At 175 A, a significant refinement of the microstructure is observed, with coarser and dense dendritic phases dominating the weld metal. The dendritic arms spacing further reduces significantly. At the highest current level of 200 A, the microstructure displays highly refined and dense dendritic phases.

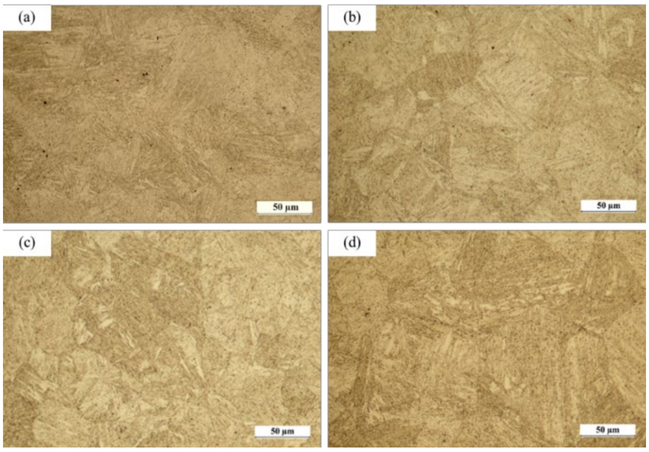

Figure 8. Microstructure of the coarse grain heat-affected zone (CGHAZ) under different welding currents (a) 125 A, (b) 150 A, (c) 175 A, and (d) 200 A.

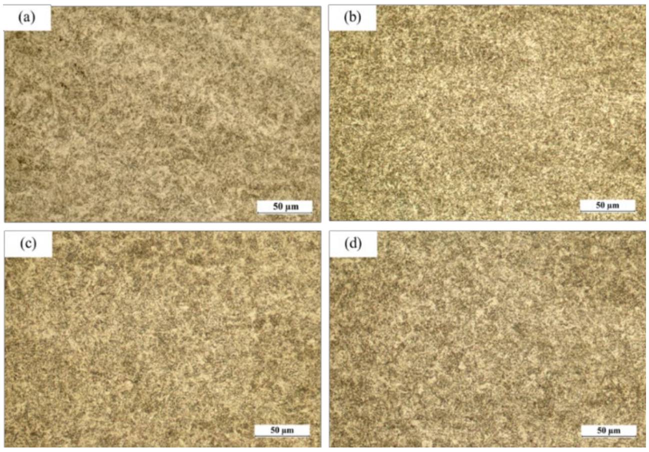

Figure 9. Microstructure of the fine grain heat-affected zone (FGHAZ) under different welding currents (a) 125 A, (b) 150 A, (c) 175 A, and (d) 200 A.

3.5 SEM characterizations

Figure 12 shows SEM images of the weld metal at different welding currents of 150 A, 175 A, and 200 A due to the effect of heat inputs on the cooling rate and microstructural evolution. The microstructure exhibited columnar dendrites consisting of primary dendrite arms (PDA) and secondary dendrite arms (SDA). It was observed that higher heat input led to a slower cooling rate, which consequently resulted in grain coarsening. At 200 A, the presence of Laves phase was detected. The primary dendrite arm spacing (PDAS) was determined by measuring the center-to-center distance between two adjacent dendrite arms, while the secondary dendrite arm spacing (SDAS) was measured as illustrated in Figure 12(a) and calculated using the following equation [44].

$$\mathrm{SDAS} = \frac{L}{N-1} \tag{4}$$

Table 5 shows the measurements of PDAS and SDAS. It was found that grain coarsening occurred with increasing welding current, leading to higher PDAS and SDAS values due to slower solidification in the interdendritic regions of the weld metal.

At a welding current of 200 A, the formation of Laves phase was observed in Figure 13. Energy-dispersive spectroscopy (EDS) analysis confirmed that the Laves phase was enriched in Nb and Mo. This was attributed to the segregation of Nb and Mo during solidification in the interdendritic region, while grain coarsening further promoted the formation of the Laves phase. The presence of Laves phases is known to increase corrosion current density and reduce overall corrosion resistance due to their higher corrosion potential compared to the γ phase [45].

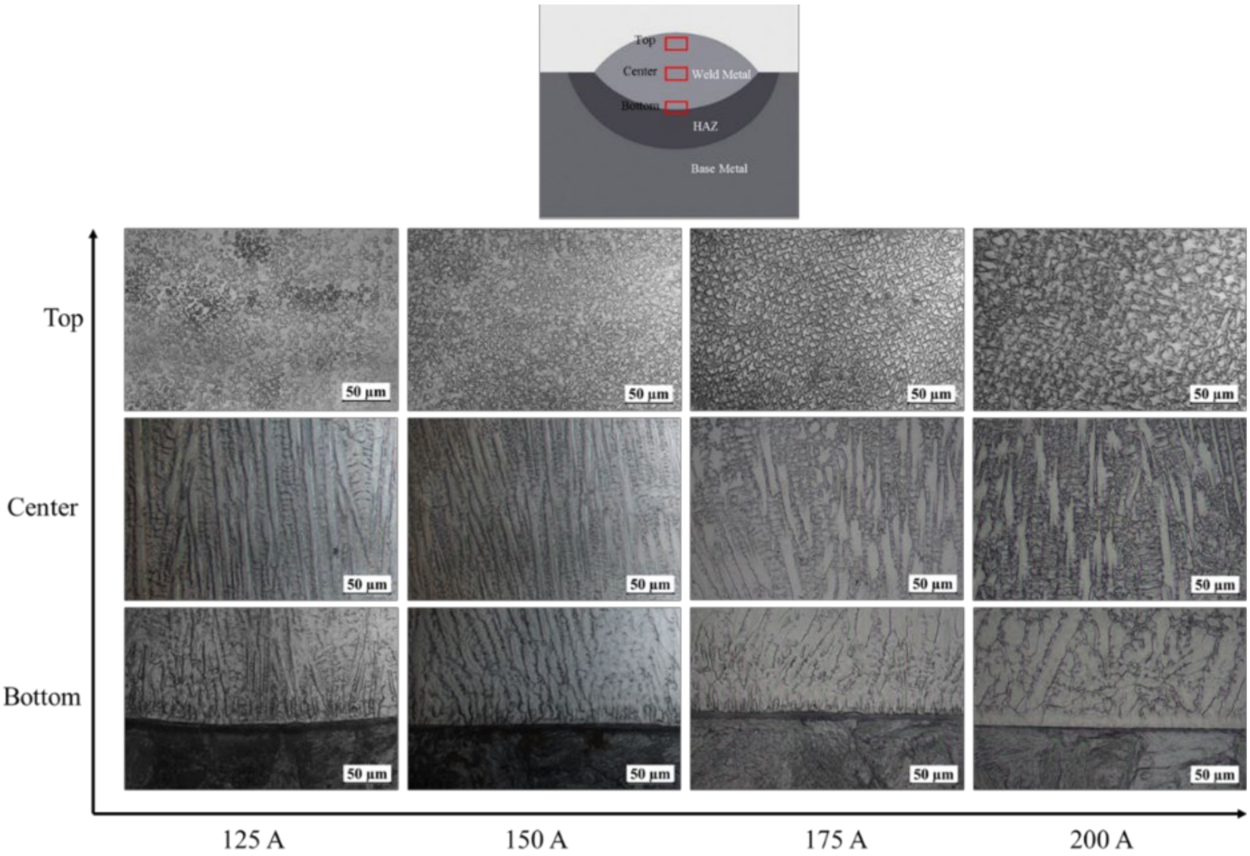

Figure 10. Microstructure of the weld metal (WM) at the top, center, and bottom under different welding currents: 125 A, 150 A, 175 A, and 200 A.

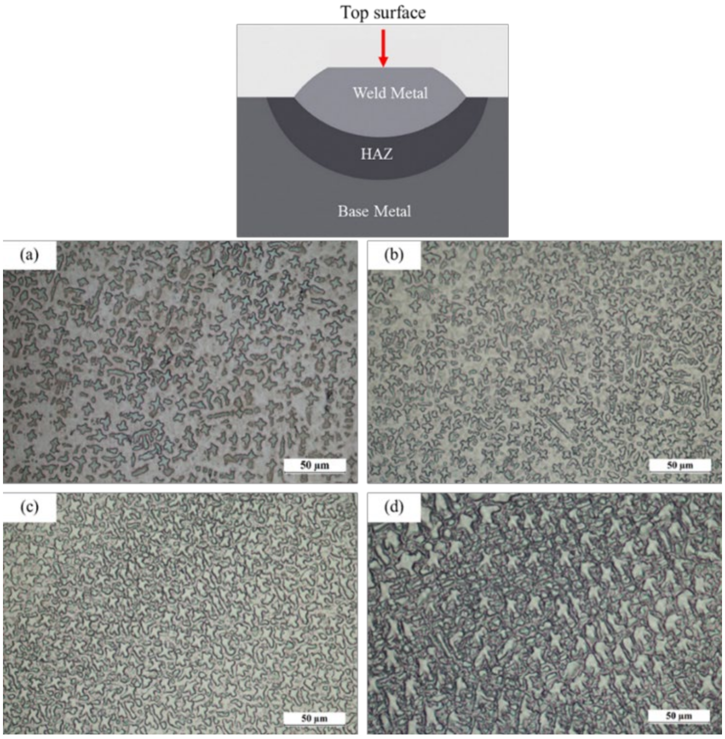

Figure 11. Microstructure of the weld metal (WM) at the top surface under different welding currents (a) 125 A, (b) 150 A, (c) 175 A, and (d) 200 A.

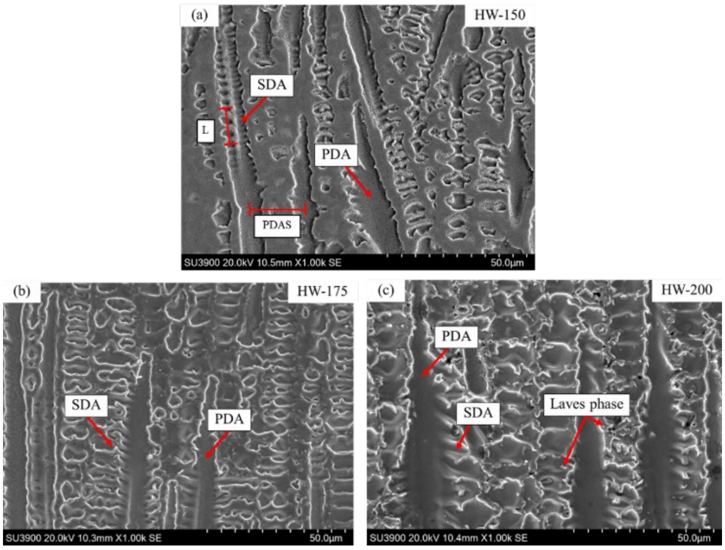

Figure 12. SEM of the weld metal (WM) at the center under different welding currents (a) 150 A, (b) 175 A, and (c) 200 A.

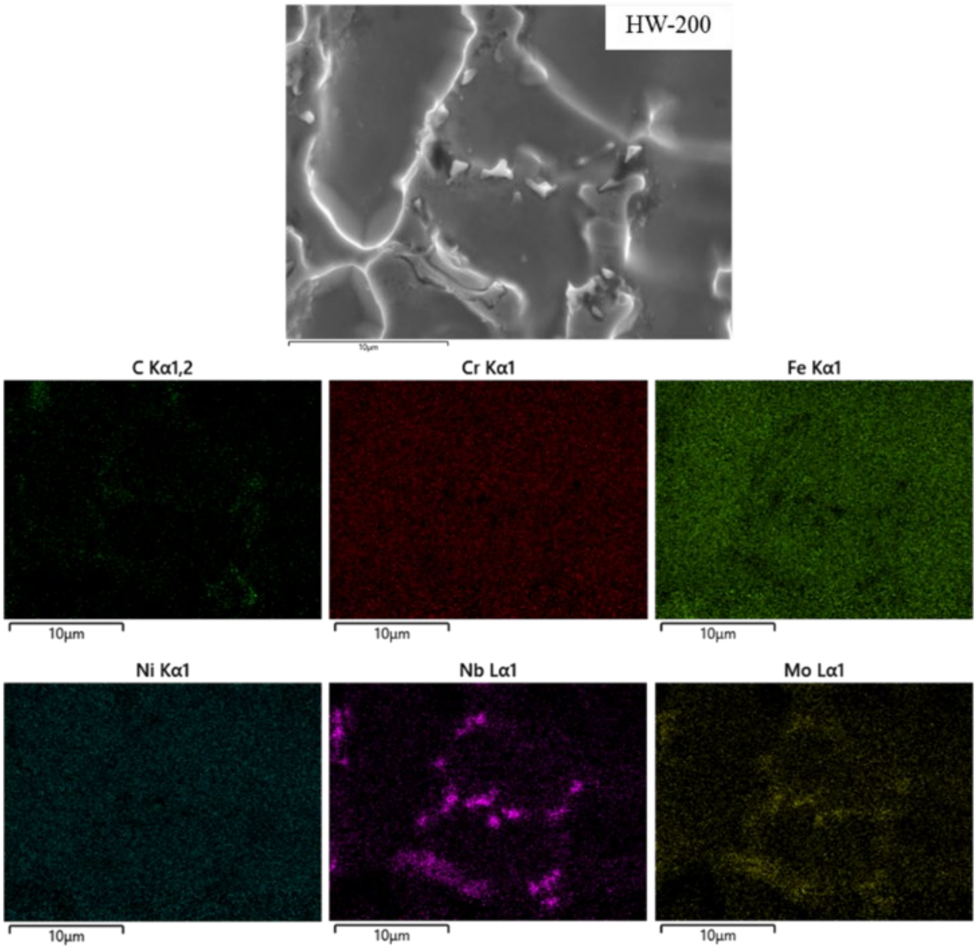

Figure 13. EDS elemental mapping of the interdendritic region in the weld metal at 200 A. The enrichment of Nb and Mo indicates the presence of Laves phase.

Table 5. Measured primary dendrite arm spacing (PDAS) and secondary dendrite arm spacing (SDAS) of the weld metal at different welding currents.

Sample	HW-150	HW-175	HW-200
PDAS [µm]	20.15	24.62	27.06
SDAS [µm]	4.24	7.25	14.63

3.6 Hardness

Figure 14 shows the variation of micro-Vickers hardness across the cross-section of the weld beads varying welding currents from 125 A to 200 A. Higher welding currents generally result in wider HAZ, as evidenced by broader peaks in the hardness profiles. The rapid cooling during welding causes the HAZ to have higher hardness than the unaffected base metal [46]. The weld metal hardness was lowest in the HW-200 sample and highest in the HW-150 sample. The HW-125 sample had the lowest HAZ hardness, while the other three samples showed similar hardness levels.

Figure 15 shows the average hardness across different regions of single weld beads. In this chart, the average hardness values for the Weld Metal (WM), Heat-Affected Zone (HAZ), and Base Metal (BM) at four different welding currents: 125 A, 150 A, 175 A, and 200 A are presented. The base metal maintained a relatively consistent hardness of approximately 209 HV across all currents because the same base metal (2.25 Cr-1Mo steel) was used for each condition. The weld metal reached its peak hardness of 240 HV when welded at 150 A, while the same region exhibited its lowest hardness of 195 HV at 200 A. In both the weld metal and HAZ, hardness generally increases from 125 A to 175 A, with the HAZ exhibiting the most significant variation. However, at 200 A, both the weld metal and HAZ show a slight decrease in hardness, suggesting a potential influence of higher heat input on the resulting microstructure and variation in the chemical elements of weld metal. The HAZ consistently displays the highest hardness values, highlighting the substantial impact of the welding thermal cycle on this region.

In Figure 16, the variation of hardness values measured on the top surface and cross-section of a weld bead at four different current levels (125 A, 150 A, 175 A, and 200 A) is shown. At 125 A and 150 A, the cross-sectional hardness is slightly higher than that of the top surface. However, at 175 A, the hardness of the top surface marginally exceeds that of the cross-section. At 200 A, cross-section hardness slightly exceeds the top surface, though both are significantly reduced. These results indicate that 150 A provides the highest hardness, whereas increasing the current beyond 150 A leads to a reduction in hardness for both top surface and cross-sectional weld bead.

3.7 Electrochemical corrosion analysis

Figure 17 shows the polarization curves obtained from testing the top surface of Inconel 625 weld metal at different welding currents. These polarization curves demonstrate the influence of welding current on the corrosion behavior of Inconel 625. The test results are summarized in Table 6. The corrosion potential (E_{corr}) indicates the initiation point of corrosion, observed at the onset of the cathodic polarization branch. The sample welded at 125 A exhibited a more negative polarization curve compared to those welded at higher currents, suggesting that corrosion reactions commenced earlier [47]. The polarization test also allows for the calculation of corrosion rate based on the corrosion current density (I_{corr}) [48]. The lowest corrosion rate was observed at 150 A, with a value of 0.506 μm/year, while the highest rate occurred at 200 A, reaching 1.077 μm/year. This indicates that the corrosion rate is dependent on current density lower current densities correspond to reduced corrosion rates [49]. In the passive region of the polarization curve, the weld produced at 200 A displayed greater stability in passive film formation compared to lower welding currents. However, increasing the welding current affects the microstructural growth and phase precipitation within the Inconel 625 weld metal, which may reduce its corrosion resistance [50].

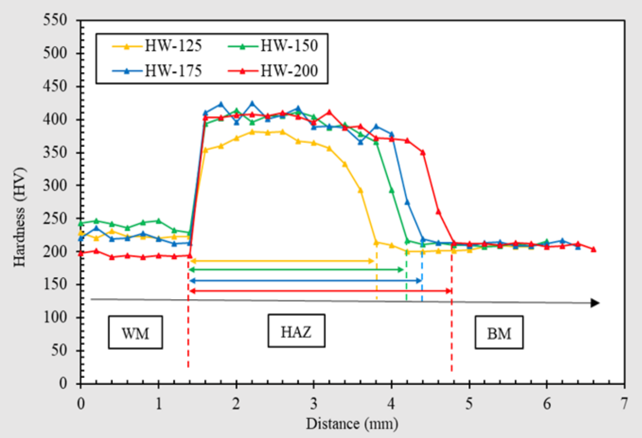

Figure 14. Hardness distributions across the weld bead under different welding currents.

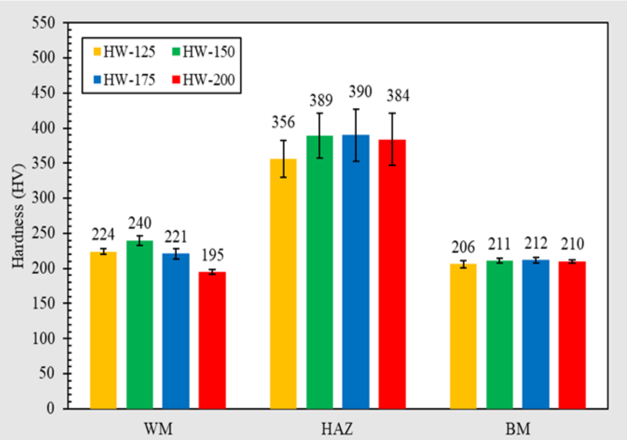

Figure 15. Average hardness in different areas under varying currents.

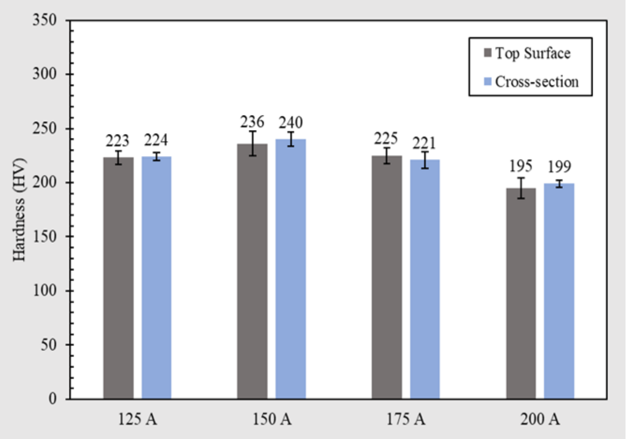

Figure 16. Average hardness of weld metal comparison between different currents.

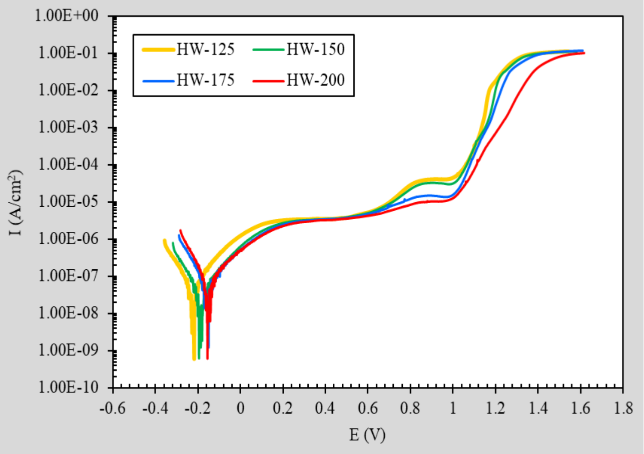

Figure 17. Polarization curves of Inconel 625 welds at different welding currents.

3.8 ANOVA analysis

Figure 18 shows the interval plot of hardness (HV) of the weld metal at different welding currents with 95% confidence intervals. It clearly shows that the welding current has an influence on the hardness properties, which is confirmed by the results of ANOVA analysis as shown in Table 7. The results prove that the welding current has a statistically significant effect on the hardness of the weld metal at the 95% confidence level ($p < 0.05$). The hardness value at 150 A is clearly different from the values at 175 A and 200 A, indicating that increasing the welding current causes a significant decrease in the hardness value. The distribution of hardness values in each group is narrow and does not overlap much, reflecting the statistical consistency of the data.

Figure 19 shows the interval plot of corrosion rate (µm/year) of the weld metal at different welding currents with 95% confidence intervals. It shows that the welding current has an influence on the corrosion rate as shown in Table 8. The ANOVA test results showed that the welding current has a statistically significant influence at the 95% confidence level ($p < 0.05$), where the value at 150 A is significantly different from the values at 175 A and 200 A. The corrosion values at 175 and 200 A are consistently higher, and the confidence intervals of each group do not overlap, indicating a clear and statistically reliable difference.

These results suggest that an optimal welding current of around 150 A provides a balance between mechanical strength and corrosion resistance. Welding at excessively high currents, while improving fusion, promotes microstructural coarsening and the formation of detrimental intermetallic phases, thereby compromising the overall weld performance.

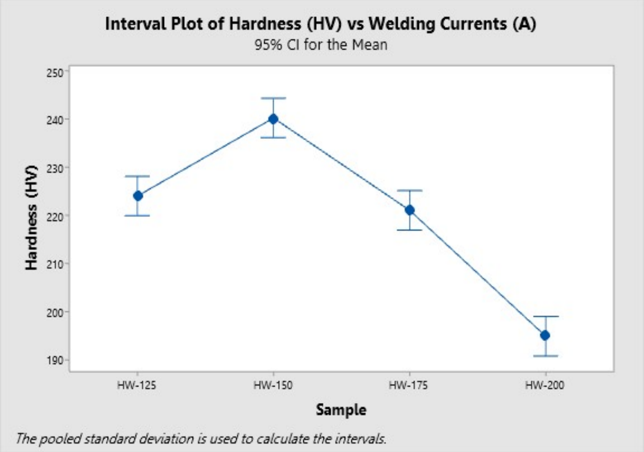

Figure 18. Interval plot of hardness (HV) of the weld metal at different welding currents with 95% confidence intervals.

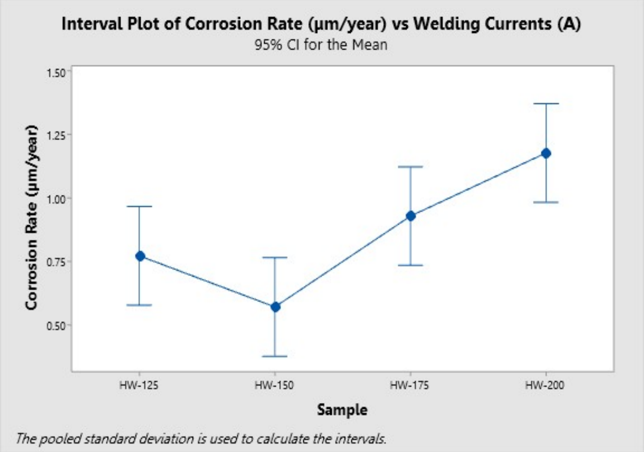

Figure 19. Interval plot of corrosion rate (µm/year) of the weld metal at different welding currents with 95% confidence intervals.

Table 6. Electrochemical corrosion results of Inconel 625 welds at different welding currents.

Samples	E_{corr} [mV]	I_{corr} [µA·cm^{-2}]	Corrosion rate [µm/year]
HW-125	-227	0.077	0.856
HW-150	-196	0.046	0.506
HW-175	-166	0.083	0.923
HW-200	-158	0.097	1.077

Table 7. Analysis of variance (ANOVA) results for the effect of welding current on hardness.

Source	DF Adj	SS Adj	MS	F-Value	P-Value	Remark
Sample	3	8427.1	2809.03	88.18	0.000	Significant
Error	28	892.0	31.86			
Total	31	9319.1				

Table 8. Analysis of variance (ANOVA) results for the effect of welding current on corrosion rate.

Source	DF Adj	SS Adj	MS	F-Value	P-Value	Remark
Sample	3	0.5878	0.19594	9.24	0.006	Significant
Error	8	0.1697	0.02121			
Total	11	0.7575				

4. Conclusions

This study revealed the influence of varying welding currents on the macrostructure, chemical composition, microstructure, mechanical properties, and corrosion resistance of the weld beads. The findings can be summarized as follows.

1. Higher welding currents significantly increased the weld bead width, HAZ size, and dilution percentage, while reducing the weld bead height. Weld dilution noticeably increased with higher welding currents, from 10% at 125 A to 15% at 150 A, then sharply increasing to 32% at 175 A, and ultimately peaking at 46% at 200 A. These results were attributed to the greater heat input at higher currents, leading to more extensive melting of the base metal.
2. X-ray fluorescence (XRF) analysis demonstrated that increasing welding current resulted in higher dilution rates, thereby altering the chemical composition of the weld beads. Notably, the concentrations of nickel, chromium, and molybdenum decreased, while the iron content from the base metal increased with higher welding currents.
3. Fine equiaxed dendrites were found at the top of the weld beads, while the center and bottom regions showed columnar structure. The microstructure of Inconel 625 weld metal varied with welding current, where lower currents (125 A, 150 A) promote fine equiaxed and thin columnar dendrites due to higher cooling rates, while higher currents (175 A, 200 A) result in coarser dendritic and columnar structures due to slower solidification.
4. The hardness profiles indicated that the HAZ exhibited the highest hardness values, whereas the weld metal's hardness peaked at 150A and decreased at 200A in both top surface and cross-sectional hardness. These variations in hardness can be related to the micro-structural changes and chemical composition alterations caused by different welding currents.
5. The corrosion results revealed that the welding current of HW-TIG process affected the corrosion behavior of the Inconel 625 weld bead. Higher currents (175 A and 200 A) exhibited increased corrosion current density (Icorr) and higher corrosion rates. In contrast, the sample produced at 150 A displayed the lowest corrosion current density and corrosion rate, indicating higher corrosion resistance compared to the samples welded at the other three welding currents.
6. According to the experimental and statistical results, the optimal welding current of 150A was identified, including a balanced combination of desirable weld characteristics, appropriate dilution levels, favorable chemical composition, microstructure, desirable hardness and corrosion resistance.

Acknowledgements

This work was supported by Faculty of Engineering, Academic Year 2024, Prince of Songkla University, Thailand. The authors would like to express their sincere gratitude to Center for Sustainable and Advanced Materials (CSAM), Faculty of Engineering, Prince of Songkla University for the financial support. The authors are grateful to Assistant Professor Muhamad Tehyo from Princess of Naradhiwas University, Thailand for helping the statistical analysis.

References

[1] J. Kuželka, M. Nesládek, M. Lutovinov, J. Jurenka, M. Růžička, M. Rund, and P. Měšťánek, "Numerical simulations of fatigue crack growth in a steam turbine rotor blade groove," *Procedia Structural Integrity*, vol. 17, pp. 780-787, 2019.

[2] M. Nesládek, M. Bartošák, J. Jurenka, J. Papuga, M. Růžička, P. Měšt'ánek, and J. Džugan, "Thermo-mechanical fatigue prediction of a steam turbine shaft," *MATEC Web of Conferences*, vol. 165, p. 22016, 2018.

[3] Z. Mazur, and A. Hernandez-Rossette, "Steam turbine rotor discs failure evaluation and repair process implementation," *Engineering Failure Analysis*, vol. 56, pp. 545-554, 2015.

[4] S. Barella, M. Bellogini, M. Boniardi, and S. Cincera, "Failure analysis of a steam turbine rotor," *Engineering Failure Analysis*, vol. 18, no. 6, pp. 1511-1519, 2011.

[5] J. Chen, and D. Jiang, "Dynamic response of steam seal rubbing in steam turbine considering thermal effect," Prognostics and System Health Management Conference (PHM-Harbin), pp. 1-6, 2017.

[6] M. Wu, Y. Zhao, and F. Meng, "The analysis and solution of contact rubbing fault for low pressure rotor of gas-steam combined cycle turbine unit." *IOP Conference Series: Earth and Environmental Science*, vol. 446, no. 2, p. 022078, 2020.

[7] C. Liu, D. Jiang, J. Chen, and J. Chen, "Torsional vibration and fatigue evaluation in repairing the worn shafting of the steam turbine," *Engineering Failure Analysis*, vol. 26, pp. 1-11, 2012.

[8] F. Tancsics, N. Légmán, L. Varga, and H. Hargitai, "Advantages of corrosion-resistant overlay welding on steel S355J2N," *Applied Sciences*, vol. 15, no. 7, pp. 3832, 2025.

[9] Y. Huang, M.-Y. Song, F.-Z. Xuan, and S. Weng, "Effect of overlaying welding repair on stress corrosion cracking sensitivity of low-pressure nuclear steam turbine rotor in the simulated environment," *Journal of Materials Engineering and Performance*, vol. 32, no. 5, pp. 2205-2217, 2023.

[10] N. Pravin Kumar, G. Sreedhar, S. Mohan Kumar, B. Girinath, A. Rajesh Kannan, R. Pramod, N. Siva Shanmugam, and M. Vishnukumar, "Microstructure and electrochemical evaluation of ER-308L weld overlays on AISI 321 stainless steel for repair applications," *Proceedings of the Institution of Mechanical Engineers, Part E: Journal of Process Mechanical Engineering*, vol. 238, no. 1, pp. 441-450, 2024.

[11] C. Borgmann, P. Dumstorff, T.-U. Kern, H. Almstedt, and K. Niepold, "Integrated weld quality concept—A holistic design

approach for steam turbine rotor weld joints," *Journal of Engineering for Gas Turbines and Power*, vol. 138, no. 4, pp. 042601, 2016.

[12] R. Donnini, A. Varone, A. Palombi, S. Spiller, P. Ferro, and G. Angella, "High energy density welding of ni-based superalloys: An overview," *Metals* (2075-4701), vol. 15, no. 1, 2025.

[13] R. G. N. Silva, A. d. S. P. Pereira, J. M. S. de Sousa, and M. Pereira, "Tribological comparison of Inconel 625 coatings deposited via laser metal deposition and tungsten inert gas welding process," *Journal of Laser Applications*, vol. 32, no. 2, 2020.

[14] E. Spaniol, T. Ungethüm, M. Trautmann, K. Andrusch, M. Hertel, and U. Füssel, "Development of a novel TIG hot-wire process for wire and arc additive manufacturing," *Welding in the World*, vol. 64, pp. 1329-1340, 2020.

[15] J. Bai, C. Fan, S. b. Lin, C. Yang, and B. Dong, "Effects of thermal cycles on microstructure evolution of 2219-Al during GTA-additive manufacturing," *The International Journal of Advanced Manufacturing Technology*, vol. 87, pp. 2615-2623, 2016.

[16] K. Shinozaki, M. Yamamoto, K. Mitsuhata, T. Nagashima, T. Kanazawa, and H. Arashin, "Bead formation and wire temperature distribution during ultra-high-speed GTA welding using pulse-heated hot-wire," *Welding in the World*, vol. 55, pp. 12-18, 2011.

[17] H. Wang, S. Hu, Z. Wang, and Q. Xu, "Arc characteristics and metal transfer modes in arcing-wire gas tungsten arc welding," *The International Journal of Advanced Manufacturing Technology*, vol. 86, pp. 925-933, 2016.

[18] R. Darji, V. Badheka, K. Mehta, J. Joshi, A. Yadav, and A. K. Chakraborty, "Investigation on stability of weld morphology, microstructure of processed zones, and weld quality assessment for hot wire gas tungsten arc welding of electrolytic tough pitch copper," *Materials and Manufacturing Processes*, vol. 37, no. 8, pp. 908-920, 2022.

[19] M. Santangelo, B. Silwal, and A. Purdy, "Vibration assisted robotic hot-wire gas tungsten arc welding (GTAW) for additive manufacturing of large metallic parts," *in Proceedings of the 26th Annual International Solid Freeform Fabrication Symposium – An Additive Manufacturing Conference*, pp. 1548-1556. 2016,

[20] A. Pai, I. Sogalad, S. Albert, P. Kumar, T. Mitra, and S. Basavarajappa, "Comparison of microstructure and properties of modified 9Cr-1Mo welds produced by narrow gap hot wire and cold wire gas tungsten arc welding processes," *Procedia Materials Science*, vol. 5, pp. 1482-1491, 2014.

[21] A. Pai, I. Sogalad, S. Basavarajappa, and P. Kumar, "Assessment of impact strength of welds produced by cold wire and hot wire gas tungsten arc welding (GTAW) processes," *Materials Today*: *Proceedings*, vol. 24, pp. 983-994, 2020.

[22] B. Silwal, and M. Santangelo, "Effect of vibration and hot-wire gas tungsten arc (GTA) on the geometric shape," *Journal of Materials Processing Technology*, vol. 251, pp. 138-145, 2018.

[23] P. Zhilin, G. Gavrilov, E. Gerasimov, and O. Melnichenko, "Advanced welding and cladding methods using auxiliary cold and hot wires," *Procedia Structural Integrity*, vol. 30, pp. 209-215, 2020.

[24] O. Muránsky, H. Zhu, S.-L. Lim, K. Short, J. Cairney, and M. Drew, "On the evolution of mechanical properties and microstructure of ferritic-bainitic (FB) 2.25 Cr-1Mo (Grade 22) steel during high-temperature creep," *Materialia*, vol. 9, pp. 100513, 2020.

[25] P. Thejasree, N. Manikandan, J. Binoj, K. Varaprasad, D. Palanisamy, and R. Raju, "Numerical simulation and experimental investigation on laser beam welding of Inconel 625," *Materials today: proceedings*, vol. 39, pp. 268-273, 2021.

[26] A. Kreitcberg, K. Inaekyan, S. Turenne, and V. Brailovski, "Temperature-and time-dependent mechanical behavior of post-treated IN625 alloy processed by laser powder bed fusion," *Journal of Manufacturing and Materials Processing*, vol. 3, no. 3, pp. 75, 2019.

[27] P. Elango, and S. Balaguru, "Welding parameters for Inconel 625 overlay on carbon steel using GMAW," *Indian Journal of Science and Technology*, vol. 8, no. 31, pp. 1-5, 2015.

[28] C. P. Alvaraes, J. C. Jorge, L. F. de Souza, L. S. Araujo, M. C. Mendes, and H. N. Farneze, "Microstructure and corrosion properties of single layer Inconel 625 weld cladding obtained by the electroslag welding process," *Journal of Materials Research and Technology*, vol. 9, no. 6, pp. 16146-16158, 2020.

[29] J. S. Kim, Y. I. Park, and H. W. Lee, "Effects of heat input on the pitting resistance of Inconel 625 welds by overlay welding," *Metals and Materials International*, vol. 21, pp. 350-355, 2015.

[30] J. H. Park, M. Cheepu, and S. M. Cho, "Analysis and characterization of the weld pool and bead geometry of Inconel 625 super-TIG welds," *Metals*, vol. 10, no. 3, pp. 365, 2020.

[31] F. Cao, S. Chen, and C. Du, "Investigation of hot-wire TIG welding based on the heat-conduction," *Energy Procedia*, vol. 144, pp. 9-15, 2018.

[32] C. Fujun, Z. Jingqi, and D. Chengchao, "Hot-wire TIG welding based on the heat-conduction," *zggx*, vol. 48, no. 6, pp. 104-109, 2023.

[33] B. Silwal, J. Walker, and D. West, "Hot-wire GTAW cladding: inconel 625 on 347 stainless steel," *The International Journal of Advanced Manufacturing Technology*, vol. 102, pp. 3839-3848, 2019.

[34] A. Evangeline, and P. Sathiya, "Structure–property relationships of Inconel 625 cladding on AISI 316L substrate produced by hot wire (HW) TIG metal deposition technique," *Materials Research Express*, vol. 6, no. 10, pp. 106539, 2019.

[35] C. Magadum, S. Ponnusamy, M. Muthukrishnan, and B. Nair, "Developments and improvements using hot wire gas tungsten arc welding–A review," *Applied Science and Engineering Progress,* vol. 16, no. 2, pp. 5965-5965, 2023.

[36] A. Fande, S. Kavishwar, V. Tandon, D. C. Narayane, and D. Bandhu, "Influence of inconel interlayer on microstructural, mechanical and electrochemical characteristics in single-pass ATIG welding of dissimilar austenitic and duplex stainless steel," *Materials Research Express*, vol. 11, no. 5, pp. 056519, 2024.

[37] A. Kumar, S. M. Pandey, and C. Pandey, "Dissimilar weldments of ferritic/martensitic grade P92 steel and Inconel 617 alloy: Role of groove geometry on mechanical properties and residual stresses," *Archives of Civil and Mechanical Engineering*, vol. 23, no. 1, p. 54, 2022.

[38] X. Xu, G. Mi, L. Chen, L. Xiong, P. Jiang, X. Shao, and C. Wang, “Research on microstructures and properties of Inconel 625 coatings obtained by laser cladding with wire,” *Journal of alloys and Compounds*, vol. 715, pp. 362-373, 2017.

[39] K. Song, Z. Wang, S. Hu, S. Zhang, and E. Liang, "Welding current influences on Inconel 625/X65 cladding interface," *Materials and Manufacturing Processes*, vol. 33, no. 7, pp. 770-777, 2018.

[40] Y. Liu, X. Xue, H. Fang, Y. Tan, H. Cui, and R. Chen, "Columnar grains formation and mechanical properties improvement of Ti44Al alloy by cyclic directional heat treatment," *Journal of Materials Research And Technology*, vol. 9, no. 6, pp. 16355-16366, 2020.

[41] C. C. Silva, H. C. De Miranda, M. F. Motta, J. P. Farias, C. R. M. Afonso, and A. J. Ramirez, "New insight on the solidification path of an alloy 625 weld overlay," *Journal of Materials research and Technology*, vol. 2, no. 3, pp. 228-237, 2013.

[42] W. Li, W. Liu, H. Liu, Z. Ma, T. Wang, G. Hu, Z. Lyu, H. Zhang, J. Song, and B. Liu, “Research and prospect on microstructure and properties of laser additive manufactured parts,” *The International Journal of Advanced Manufacturing Technology*, vol. 130, no. 5, pp. 2023-2064, 2024.

[43] L. Guo, F. Xiao, F. Wang, W. Wei, Y. He, and F. Luo, “Influence of heat treatments on microstructure, mechanical properties and corrosion resistance of Inconel 625 overlay cladded using PTIG,” *Materials Research Express*, vol. 7, no. 9, pp. 096517, 2020.

[44] C. Zhang, Z. Qiu, H. Zhu, Z. Wang, O. Muránsky, M. Ionescu, Z. Pan, J. Xi, and H. Li, “On the effect of heat input and interpass temperature on the performance of inconel 625 alloy deposited using wire arc additive manufacturing–cold metal transfer process,” *Metals*, vol. 12, no. 1, pp. 46, 2021.

[45] X. You, Y. Tan, L. Zhao, Q. You, Y. Wang, F. Ye, and J. Li, “Effect of solution heat treatment on microstructure and electrochemical behavior of electron beam smelted Inconel 718 superalloy,” *Journal of Alloys and Compounds*, vol. 741, pp. 792-803, 2018.

[46] L. Tsay, C. Liu, Y.-H. Chao, and Y. Shieh, “Fatigue crack propagation in 2.25 Cr–1.0 Mo steel weldments in air and hydrogen,” *Materials Science and Engineering*: A, vol. 299, no. 1-2, pp. 16-26, 2001.

[47] G. d. S. Vacchi, R. Silva, C. L. Kugelmeier, C. B. M. Junior, I. Dainezi, J. H. Alano, A. d. A. Mendes Filho, W. R. Ramos Osorio, and C. A. Della Rovere, “Corrosion behavior of CW6MC nickel cast alloy (Inconel 625) welded by shielded metal arc welding,” *Metals*, vol. 11, no. 8, pp. 1286, 2021.

[48] K. Łyczkowska, and J. Michalska, “Studies on the corrosion resistance of laser-welded Inconel 600 and Inconel 625 nickel-based superalloys,” *Archives of Metallurgy and Materials*, vol. 62, 2017.

[49] F. Ostovan, E. Hasanzadeh, M. Toozandehjani, E. Shafiei, K. R. Jamaluddin, and A. Amrin, “Microstructure, hardness and corrosion behavior of gas tungsten arc welding clad Inconel 625 super alloy over A517 carbon steel using ERNiCrMo$_3$ filler metal,” *Journal of Materials Engineering and Performance*, vol. 29, pp. 6919-6930, 2020.

[50] J.-S. Kim, and H.-W. Lee, “A study on effect of intergranular corrosion by heat input on Inconel 625 overlay weld metal,” *International Journal of Electrochemical Science*, vol. 10, no. 8, pp. 6454-6464, 2015.